PHYSICAL REVIEW E **76**, 046211 (2007)

Steady-state solutions to the advection-diffusion equation and ghost coordinates for a chaotic flow

S. R. Hudson
Princeton Plasma Physics Laboratory, P.O. Box 451, Princeton, New Jersey 08543, USA

(Received 12 December 2006; published 10 October 2007)

Steady-state solutions to the advection-diffusion equation for a passive scalar, with a chaotic divergence-free flow, are determined using a discrete-time, finite-difference model. The physical system studied is a density of particles diffusing across a chaotic layer. The impact of the advective structures on the solutions is illustrated, with special attention given to the cantori. It is argued that cantori play an important role in restricting transport and that coordinates adapted to cantori, called ghost coordinates, provide a natural framework about which the dynamics may be organized; for example, the averaged density profile becomes a smoothed devil's staircase in ghost coordinates.

DOI: 10.1103/PhysRevE.76.046211 PACS number(s): 89.75.Kd, 47.52.+j

I. INTRODUCTION

In this article we study advective-diffusive transport in a chaotic flow, as described by

$$\frac{\partial \rho}{\partial t} + \mathbf{v} \cdot \boldsymbol{\nabla} \rho = D \nabla^2 \rho, \tag{1}$$

where $\rho(\mathbf{x},t)$ is a scalar quantity—for example, a particle density—that depends on both position $\mathbf{x}$ and time t, that is advected by the velocity field $\mathbf{v}$, and that diffuses with diffusion constant D. This equation arises in many areas of physics, including fluid mechanics, plasma physics, and chemical kinetics and has a long history [1], predating recent developments in chaos theory such as the Kolmogorov-Arnold-Moser (KAM) theorem [2–5]. In this article we consider the case where the scalar is passive (the transport of ρ does not affect $\mathbf{v}$) and where the flow is divergence free, constant in time, and possesses a mix of regular and irregular streamlines. The primary focus of this article is to investigate which structures of the chaotic flow affect the steady-state density for small but nonzero D and to what extent coordinates adapted to the invariant structures of the chaotic flow (namely, the periodic orbits and noble cantori) can be used to "straighten out" the steady-state density contours.

Divergence-free flows can be written $\mathbf{v}=\boldsymbol{\nabla}\times\mathbf{A}$, where $\mathbf{A}=A_x\boldsymbol{\nabla}x+A_y\boldsymbol{\nabla}y+A_z\boldsymbol{\nabla}z$, where A_x, A_y, and A_z are functions of the coordinates (x,y,z). Using the gauge freedom to set $A_y=0$ and making the canonical choice of (radial) momentum coordinate $y=A_x$ so that $\mathbf{A}=y\boldsymbol{\nabla}x-H(x,y,z)\boldsymbol{\nabla}z$, the trajectory of a streamline is given by $\dot{x}=\partial_y H$ and $\dot{y}=-\partial_x H$, where the overdot denotes the derivative with respect to z. These are simply Hamilton's equations, where x, y, and z are analogous to the position, canonical momentum, and time (assumed periodic) and the advective flow is analogous to a $1\frac{1}{2}$-dimensional Hamiltonian system.

If the Hamiltonian flow is integrable, the streamlines lie on invariant surfaces and the advective dynamics is reduced to simple linear motion by constructing a coordinate system with a momentum *action* coordinate that is adapted to the invariant surfaces, and thus remains constant, and a position *angle* coordinate that increases linearly in time [6]. However, Hamiltonian flows are typically chaotic. Regular trajectories and invariant surfaces are intermixed with irregular trajectories that fill a volume [4,5,7], and for such systems action-angle coordinates cannot be *everywhere* constructed in three-dimensional phase space; however, they can be *locally* constructed.

For slightly chaotic systems, there remain a finite measure of invariant KAM surfaces. By suitably adapting the coordinates [8], the motion on these surfaces can be reduced to simple linear motion. Between the KAM surfaces the motion is complicated and no coordinates can completely straighten out the chaos, but the motion is not random. Even in strongly chaotic regions where no KAM surfaces are present, there remain invariant sets, such as the periodic orbits, on which the motion is regular. Coordinates may be adapted to these structures. Perhaps the most important structures in a chaotic layer are the cantori, as the cantori create *partial barriers* to radial transport within the chaotic layer.

In this article we illustrate a coordinate system adapted to a selection of periodic orbits of a chaotic flow. By choosing periodic orbits that approximate a preferred set of cantori, the partial barriers themselves coincide with coordinate curves. Such coordinates can organize the chaotic advective dynamics by partitioning phase space into regions of rapid mixing that are separated by the partial barriers.

Regarding the steady-state solutions to the advection-diffusion equation, some statements can readily be made. For large D, the diffusion dominates: the solution will be smooth and is primarily determined by the boundary conditions. In the opposite limit $D=0$, the dynamics is determined by the advection alone and the steady-state density is constant along a streamline, $\mathbf{v}\cdot\boldsymbol{\nabla}\rho=0$. In this case, the density on points located on different streamlines are independent. For chaotic flows, where different streamlines in the stochastic sea mix and tangle together in an exceedingly complicated fashion, the solution will have structure on all length scales (depending on the initial conditions).

It is the intermediate case, where D is small but nonzero, that is of present interest. Any diffusion (including artificial diffusion due to finite numerical resolution) will smooth out the intricate structure, but for small D one may expect that the structures of the advective flow will still dominate the steady-state solution.

It is well known in fluid mechanics that the unstable manifold has an important effect on the solutions. The unstable manifold was known to Poincaré [9]. Detailed studies of transport in Hamiltonian systems are based on the dynamics of the "lobes" of the heteroclinic tangle [10,11]. The unstable manifold leads to *enhanced* mixing near the unstable periodic orbits in chaotic advection [12–15]. In a different context, the geometry of the unstable manifold is related to the heat "footprint" in diverted tokamaks and that enhancement of the stochastic layer of the unstable manifold can lead to a favorable suppression of edge-localized plasma instabilities [16].

There are other structures which have an important effect on transport—namely, the KAM surfaces and the islands embedded within the chaotic sea. The advective flux across a KAM surface is zero, so the only transport across these surfaces (or into the islands) is diffusive. The KAM surfaces, however, are ultimately destroyed as the chaos increases, and the elliptic invariant surfaces around stable periodic orbits do not restrict radial transport. The question then arises, what structures *inhibit* the advective-diffusive transport where no KAM surfaces are present?

An obvious candidate for investigation is the cantorus: the remnant, invariant set with irrational frequency surviving after destruction of a KAM surface [17–19]. Although the cantori are "leaky," the near-critical cantori in particular create partial barriers that can severely restrict Hamiltonian transport [20,21]. It is not obvious that cantori will play a significant role in diffusive systems: cantori are zero-dimensional sets (in two-dimensional phase space) [22,23], and the dynamics may be overwhelmed by the combined effects of diffusion and the enhanced mixing provided by the unstable manifolds comprising the surrounding stochastic sea.

This article shall suggest that the cantori do play an important role and that coordinates adapted to the cantori can organize the advective-diffusive dynamics. Steady-state solutions to the advection-diffusion equation are determined using a discrete-time, finite-difference model, described in Sec. II. The physical system mimicked is that of particles diffusing across a chaotic layer, bounded by KAM surfaces, where the standard map [24,25] is used to model the advective flow. The correlation between the density contours and the unstable manifolds is illustrated graphically in Sec. III, along with the presentation that there is a critical island width above which the advection dominates the diffusion and the density is flattened across the island.

Also, graphical evidence is given that the steady-state density contours coincide with noble cantori, which are the most important barriers to the advective transport. This suggests that a coordinate system where the cantori lie on coordinate curves will organize the dynamics. A coordinate system based on *ghost circles* [26,27], curves that connect the minimax and minimizing periodic orbits, is constructed in Sec. IV. By choosing ghost circles that approximate the noble cantori, ghost coordinates provide a framework about which the chaotic, fractal structure of the solution may be perceived and a devil's staircase [28] property of the solution is revealed.

II. DISCRETE-TIME, FINITE-DIFFERENCE MODEL

To explore the steady-state solutions to the advection-diffusion equation, with chaotic, divergence-free flows, a discrete-time, curvilinear finite-difference model is adopted.

A common approach in the study of Hamiltonian flows is to consider the successive intersections of a streamline with a plane, a Poincaré section, that is transverse to the flow. The dimensionality of the system is reduced, and the dynamics is then given by an area-preserving map $\mathbf{x}_{i+1}=T(\mathbf{x}_i)$, where $\mathbf{x}=(x,y)$. In general, given $H(x,y,z)$, the mapping T must be constructed numerically by integrating Hamilton's equations over one z period.

It is much simpler if one is given the map directly. In this article we consider the case where the Hamiltonian "flow" is given by the standard map [24,25]

$$T\begin{pmatrix} x \\ y \end{pmatrix} = \begin{pmatrix} x + y - k\,\sin(2\pi x)/2\pi \\ y - k\,\sin(2\pi x)/2\pi \end{pmatrix}, \tag{2}$$

where k is a perturbation parameter.

The mapping has a variational formulation. For an arbitrary "trial" trajectory, represented as a sequence of position coordinates $\{x_i\}$, the action is given by

$$W = \sum_i h(x_i, x_{i+1}), \tag{3}$$

where $h(x_i,x_{i+1})=\frac{1}{2}(x_{i+1}-x_i)^2+k\,\cos(2\pi x_i)/4\pi^2$. Trajectories are stationary points of the action, where the action gradient

$$\frac{\partial W}{\partial x_i} = (x_i - x_{i-1}) + (x_i - x_{i+1}) - k\,\sin(2\pi x_i)/2\pi \tag{4}$$

is zero. By identifying $y_{i+1}=x_{i+1}-x_i$, the mapping, Eq. (2), is recovered. Action-extremizing techniques provide an efficient means for locating periodic orbits for both the discrete-time [29] and continuous-time [30] cases, even for the high-order periodic orbits that approximate the cantori. The action restricted to (p,q) periodic orbits is denoted $W_{p/q}$. Periodic orbits will be written as $\{x_i,\ i=0,\ q-1\}$, with $x_{i+q}=x_i+p$, when the action formalism is used, and $\{(x_i,y_i),\ i=0,\ q-1\}$, with $x_{i+q}=x_i+p$ and $y_{i+q}=y_i$ otherwise. The action formalism is also used to define the ghost circles [26,27], as will be described in Sec. IV.

For $k=0$, the coordinates (x,y) are essentially action-angle coordinates: phase space is foliated by invariant curves $y=\text{const}$, on which the angle coordinate x increases at a constant "frequency," $\omega=\lim_{n\to\infty}(x_n-x_0)/n$, which may be rational or irrational. An irrational curve is the closure of a single trajectory with irrational frequency, whereas a rational curve is a family of periodic trajectories with frequency $\omega=p/q$, for integers p and q. For k nonzero, the rational curves break into chains of islands, and typically only the hyperbolic, action-minimizing periodic orbit and the elliptic, action-minimax periodic orbit survive [4,5]. Chaotic trajectories emerge near the hyperbolic orbit, but the elliptic orbits are shielded, for small k, from the chaos by the formation of islands, which form regions of predominantly stable, regular motion.

The irrational trajectories are quite robust to perturbation [18], although their closure is not always a continuous curve. For small perturbations (how small depends on the "irrationality" of the frequency), the closure remains a smooth curve, called a KAM curve [2–5], and presents a complete barrier to radial advective transport. As the perturbation exceeds a critical value, the smooth curve disintegrates and develops the structure of a Cantor set, with an infinite sequence of "gaps," and is called a cantorus [17]. Although the cantori are "leaky," it can take an extremely long time for trajectories to pass through near-critical cantori, and these cantori create very strong barriers to Hamiltonian transport in regions of chaos.

The standard map is often used to study chaotic systems with "twist" (monotonic velocity profile) [7]. (For systems with nonmonotonic profile, the nontwist map may be used [31,32].) It displays many of the characteristic features of continuous-time systems, such as the existence and breakup of KAM curves and the presence of islands and chaotic regions. In particular, it was recently shown [30] that the flux across near-critical noble cantori of a Hamiltonian flow satisfies the same scaling relation as that for the standard map.

The utility of replacing the continuous flow with a discrete map is that the computational burden is diminished and greater numerical resolution in the two-dimensional plane is afforded. As the mapping is periodic in the x coordinate, the domain may be restricted to $x \in (-\frac{1}{2}, \frac{1}{2}]$. The standard map satisfies the symmetry $T(-\mathbf{x}) = -T(\mathbf{x})$. If symmetric boundary conditions are chosen, the density satisfies $\rho(-\mathbf{x}) = -\rho(\mathbf{x})$. This allows the computational domain to be reduced to $x \in [0, \frac{1}{2}]$.

The chaotic layer considered here is bounded below and above by the KAM curves $\mathbf{x}_l(\alpha)$ and $\mathbf{x}_u(\alpha)$, where α is an angle parametrization. These are chosen to be the KAM curves with frequency given by $\omega_u = 1/\gamma = 0.618\,03\ldots$, where γ is the golden mean and its symmetric opposite $\omega_l = -\omega_u$. These KAM curves exist for $k < 0.9716\ldots$ (as estimated by Greene's residue criterion [25]). They are constructed by locally determining the action-angle coordinate transformation $x = x(\alpha)$ and $y = y(\alpha)$, which reduces the mapping to a rigid rotation in the angle coordinate $\alpha \to \alpha + \omega$ [8]. The boundary conditions chosen are that the density is constant on each of these curves, and to satisfy symmetry we choose $\rho_l = \omega_u$ and $\rho_u = \omega_l$, where $\rho_{l,u}$ are the densities on the lower and upper boundaries. The average density gradient is then $\Delta\rho/\Delta\omega = -1$. To implement these conditions numerically, it is convenient to employ general curvilinear coordinates that are adapted to the bounding KAM curves.

A coordinate transformation $\mathbf{x} = \mathbf{C}(\boldsymbol{\alpha})$, where $\boldsymbol{\alpha} = (\alpha, s)$, is constructed between these curves by radial interpolation:

$$\mathbf{x}(\alpha, s) = \frac{\omega_u - s}{\omega_u - \omega_l}\mathbf{x}_l(\alpha) + \frac{s - \omega_l}{\omega_u - \omega_l}\mathbf{x}_u(\alpha), \tag{5}$$

where $s \in [\omega_l, \omega_u]$ is chosen to coincide with the frequency on the bounding KAM curves. A grid $\boldsymbol{\alpha}_{i,j} = (\alpha_{i,j}, s_{i,j})$ is constructed equally spaced in both α and s: $\alpha_{i,j} = ih_\alpha$ and $s_{i,j} = s_l + jh_s$, with grid spacing $h_\alpha = 1/2N$ and $h_s = (\omega_u - \omega_l)/2N$, and N is the numerical grid resolution. The boundary conditions now take the simple form $\rho_{i,j} = \rho_1$ for $j = -N$ and $\rho_{i,j} = \rho_2$ for $j = N$, and the combined constraints of symmetry and periodicity require $\rho_{-1,j} = -\rho_{1,-j}$ and $\rho_{N+1,j} = -\rho_{1-N,-j}$, where $\rho_{N+1,j}$ lies on the "pseudo-grid-point" outside the computational domain.

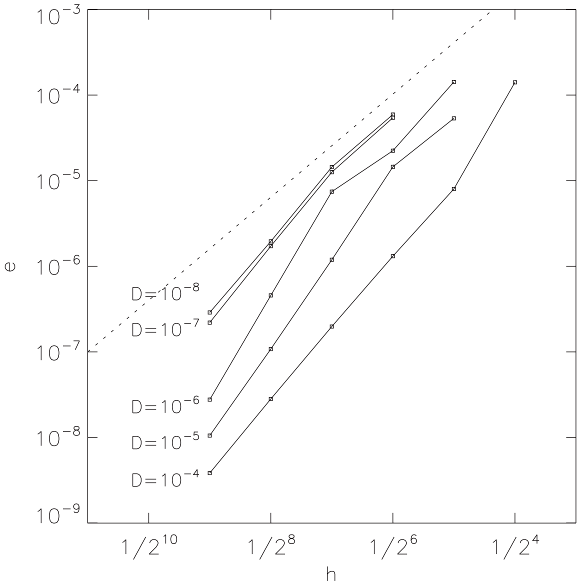

FIG. 1. Finite numerical resolution error e, scaling for various D, plotted against grid size h, for $k = 0.9716$. The dashed line satisfies $e \sim h^2$.

To solve for the temporal evolution of the advection diffusion, the method of operator splitting can be applied [33]: the scalar is first advected by the mapping, $\rho^{n+1/2}(\mathbf{x}) = \mathcal{A}\rho^n(\mathbf{x})$, and then the scalar diffuses, $\rho^{n+1}(\mathbf{x}) = \mathcal{D}\rho^{n+1/2}(\mathbf{x})$.

The advection $\partial_t \rho + \mathbf{v} \cdot \boldsymbol{\nabla} \rho = 0$ simply carries the scalar along with the flow, or in this case carries the scalar one "time step" of the mapping:

$$\mathcal{A}\rho^n(\mathbf{x}) = \rho^n(T^{-1}\mathbf{x}). \tag{6}$$

For each grid point $\boldsymbol{\alpha}_{i,j}$, the Cartesian coordinates are computed $\mathbf{x}_{i,j} = \mathbf{C}(\boldsymbol{\alpha}_{i,j})$, the mapping is inverted $T(\mathbf{x}'_{i,j}) = \mathbf{x}_{i,j}$, and the coordinate transformation is inverted $\mathbf{C}(\boldsymbol{\alpha}'_{i,j}) = \mathbf{x}'_{i,j}$. To then estimate $\rho(\boldsymbol{\alpha}'_{i,j})$, bilinear interpolation is used. The advection operation may be expressed $\rho^{n+1/2} = L_{\mathcal{A}}\rho^n + B_{\mathcal{A}}$, where $B_{\mathcal{A}}$ is a boundary term arising from the bilinear interpolation of points $\boldsymbol{\alpha}'_{i,j}$ near the computational boundary.

The diffusive operator is determined by assuming that the advective flow is far greater than the parallel diffusive flow, so that the diffusion operator is two dimensional—i.e., in the Poincaré section. The Laplacian is

$$\nabla^2 \rho = \sqrt{g}^{-1}[\partial_\alpha(\sqrt{g}\rho^\alpha) + \partial_s(\sqrt{g}\rho^s)], \tag{7}$$

where $\rho^\alpha = g^{\alpha\alpha}\rho_\alpha + g^{\alpha s}\rho_s$ and $\rho^s = g^{s\alpha}\rho_\alpha + g^{ss}\rho_s$, where $\rho_\alpha = \partial\rho/\partial\alpha$ and $\rho_s = \partial\rho/\partial s$, the "raising" metric elements are $g^{ab} = \boldsymbol{\nabla} a \cdot \boldsymbol{\nabla} b$, and $\sqrt{g}$ is the coordinate Jacobian. The derivatives ρ_α and ρ_s are calculated on the "half-grid":

$$\rho_\alpha|_{i+1/2,j+1/2} = \frac{(\rho_{i+1,j+1} + \rho_{i+1,j} - \rho_{i,j+1} - \rho_{i,j})}{2h_\alpha}, \tag{8}$$

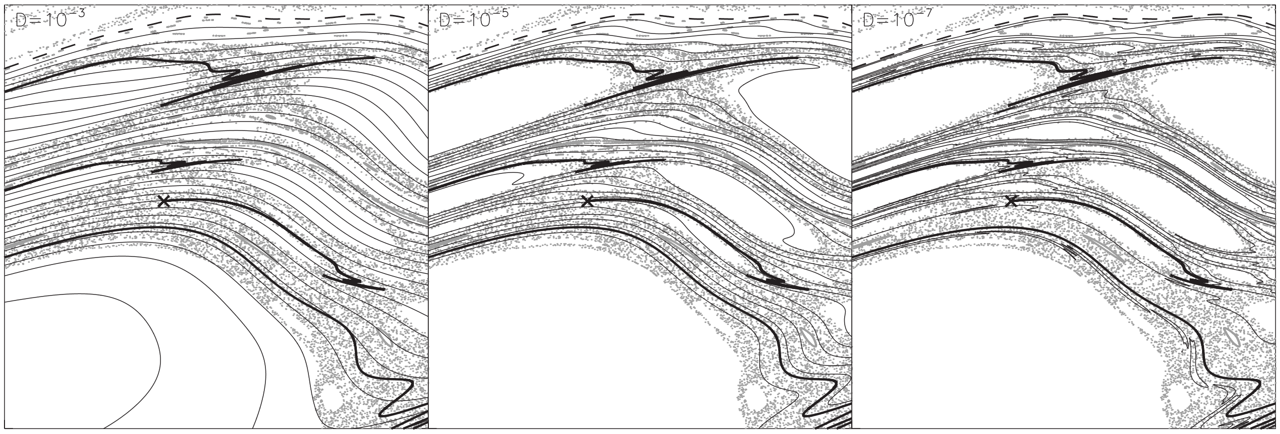

FIG. 2. Poincaré plot showing the stochastic sea (gray dots), a segment of the unstable manifolds (thick line) emanating from the (0, 1), (1, 2), (1, 3), and (1, 4) periodic orbits (×), and the density contours (black lines) for $D=10^{-3}$ (left), $D=10^{-5}$ (middle), and $D=10^{-7}$ (right). The horizontal x axis is [0.0, 0.5], the vertical y axis is [0.0, 0.7], and the perturbation parameter $k=0.9716$.

$$\rho_s|_{i+1/2,j+1/2} = \frac{(\rho_{i+1,j+1} - \rho_{i+1,j} + \rho_{i,j+1} - \rho_{i,j})}{2h_s}, \tag{9}$$

as are the metric elements $\sqrt{g}g^{\alpha\alpha}$, $\sqrt{g}g^{\alpha s}$, and $\sqrt{g}g^{ss}$. These are combined to construct the diffusion operator on the full grid—for example,

$$\begin{aligned} 2h_\alpha\partial_\alpha(\sqrt{g}g^{\alpha\alpha}\rho_\alpha)|_{i,j} = {} & \sqrt{g}g^{\alpha\alpha}\rho_\alpha|_{i+1/2,j+1/2} + \sqrt{g}g^{\alpha\alpha}\rho_\alpha|_{i+1/2,j-1/2} \\ & - \sqrt{g}g^{\alpha\alpha}\rho_\alpha|_{i-1/2,j+1/2} \\ & - \sqrt{g}g^{\alpha\alpha}\rho_\alpha|_{i-1/2,j-1/2}. \end{aligned} \tag{10}$$

This discretization is similar to that described by Günter *et al.* [34] (alternative numerical methods have been developed [35–37]). The diffusion $\partial_t\rho=D\nabla^2\rho$ is solved implicitly:

$$\rho^{n+1}_{i,j} - \rho^{n+1/2}_{i,j} = D\ \nabla^2\rho^{n+1}_{i,j}\Delta t, \tag{11}$$

where the term Δt is equal to the time step of the mapping (hereafter set equal to 1) and is included to remind the reader of the discrete-time nature of the model. The diffusion operation is written $L_{\mathcal{D}}\rho^{n+1}+B_{\mathcal{D}}=\rho^{n+1/2}$, and the total advection-diffusion temporal evolution operator is given as

$$L_{\mathcal{D}}\rho^{n+1} + B_{\mathcal{D}} = L_{\mathcal{A}}\rho^n + B_{\mathcal{A}}. \tag{12}$$

One may iterate this equation to relax an initial system to the steady state. It is, however, far quicker to set $\rho^{n+1}=\rho^n$ and solve for the steady state directly. In this case, the discretized advection balances the discretized diffusion and it is just required to solve the linear system $(L_{\mathcal{D}}-L_{\mathcal{A}})\rho=B_{\mathcal{A}}-B_{\mathcal{D}}$.

The numerical approach can easily be extended to a continuous-time system by including additional Poincaré sections between that implicitly defined by the mapping, Eq. (2). Thus, the discrete-time model employed here is similar to a finite-resolution realization of a continuous-time model; however, a detailed comparison between the discrete-time model and its continuous-time counterpart is left for future work.

The numerical resolution required is dependent on the level of diffusion. Chaotic flows have structure on all length scales. The finite-difference approach provides a simple global approximation, but it cannot resolve structures with length scale less than h. Diffusion is a smoothing operation; however, as the diffusion decreases the resolution required increases. For the following results, grid resolutions up to $N=2^{11}$ in each dimension are used. The vector of unknown quantities, $\rho_{i,j}$, has length $O(N^2)$. While the diffusion operator $L_{\mathcal{D}}$ has a simple structure, coupling only several nearest-neighbor grid points, that could be exploited for efficiency, the advective operator $L_{\mathcal{A}}$ does not. If the operator $L_{\mathcal{D}}-L_{\mathcal{A}}$ were represented as a square matrix, it would have dimension $O(N^4)$ and could not even be stored in memory on most machines. Fortunately, the operator $L_{\mathcal{D}}-L_{\mathcal{A}}$ is sparse and Krylov methods that require only the product $(L_{\mathcal{D}}-L_{\mathcal{A}})\rho$, a vector of length $O(N^2)$, are suitable. In the following results, the bi-conjugate gradient stabilized (Bi-CGSTAB) method [38] is iterated until the root-mean-square error in the solution, at a given N, is less than the tolerance 10^{-14}. The scaling of the numerical resolution error e, defined as the root mean square of the difference between the midpoint interpolated solution at resolution N and higher-resolution $2N$ values, is shown in Fig. 1 for various values of D.

III. STRUCTURE OF THE STEADY-STATE SOLUTION

To begin, the density contours for the case $k=0.9716$, with various levels of diffusion, are shown in Fig. 2. For this value of k, the computational domain is almost totally filled by stochastic field lines and islands. For large diffusion, the solution is insensitive to the fine-scale structure of the advection. As the diffusion decreases, the density contours coincide more closely with the advective structures. In particular, the density is flattened inside the island chains and, perhaps most strikingly, is influenced by the multiple unstable manifolds that comprise the irregular component.

Shown in Fig. 2 are the first few "lobes" of the unstable manifolds of the (0, 1), (1, 2), (1, 3), and (1, 4) hyperbolic periodic orbits, $\mathbf{x}_{p/q}$, where the eigenvalues λ_u and λ_s of the full-periodicity tangent map $\nabla T_{p/q}=\Pi_{i=1}^{q}\nabla T(\mathbf{x}_i)$ are real reciprocals [7]. The unstable manifolds may be computed (for

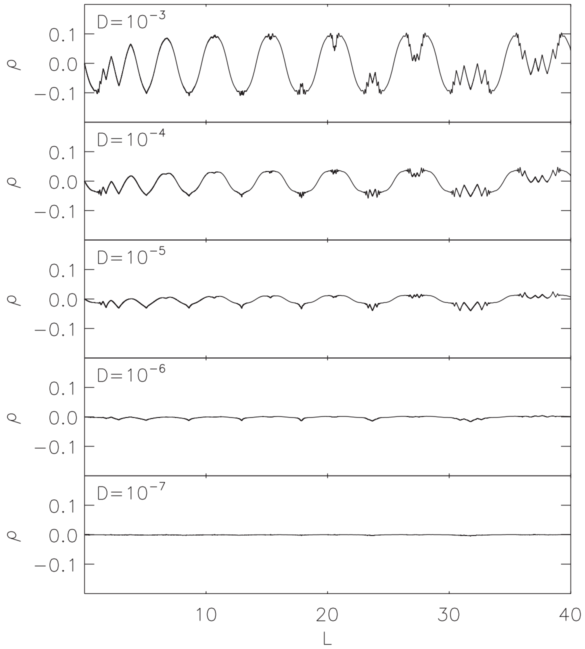

FIG. 3. Density along the (0,1) unstable manifold, plotted against length from the (0,1) unstable periodic orbit, for the perturbation parameter $k=0.9716$, and various values of diffusion D.

some distance at least, until the exponential magnification of numerical error overwhelms the calculation) by mapping a short line segment emanating from the hyperbolic periodic orbit in the unstable direction, $\mathbf{v}_u$, where $\nabla T_{p/q}\mathbf{v}_u=\lambda_u\mathbf{v}_u$ and $\lambda_u>1$. (The unstable manifold W^u associated with a hyperbolic periodic orbit is formally defined as the set of points that approach the periodic orbit *backward* in time: $\mathbf{x}\in W^u \Rightarrow T^n\mathbf{x}\rightarrow\mathbf{x}_{p/q}$ as $n\rightarrow-\infty$.)

As D decreases, the density contours are influenced not only by the "primary" unstable manifold associated with the (0,1) unstable periodic orbit, but also by the unstable manifolds associated with additional, higher-order unstable periodic orbits inside the stochastic sea, and for decreasing D give increasing structure to the solution. Shown in Fig. 3 is the density along the (0, 1) unstable manifold. As D decreases, the density tends to flatten along the unstable manifold: if coordinates could be constructed that "straightened out" the unstable manifold, then perhaps the solution could also be straightened out to some degree. However, the unstable manifolds quickly develop wild oscillations that lie at the heart of the complexity of chaotic systems: it seems unlikely that a coordinate system adapted to this structure could be globally well defined.

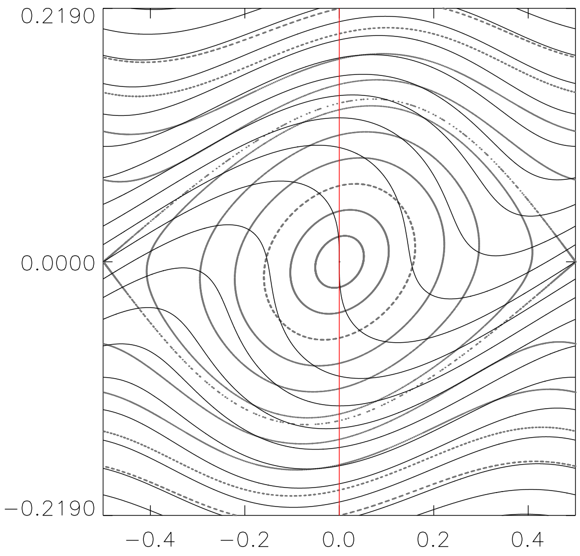

FIG. 4. (Color online) Density contours (black lines), showing the density inflection, and Poincaré plot (gray dots), across the (0,1) island, for $D=10^{-3}$ and $k=0.191787$.

Regarding the flattening of the density across the islands, there exists a critical island width W, given by the balance of the advection with the diffusion, above which the density is flattened across the island. The radial variation in the advection operation scales linearly with radial variation Δy, whereas the diffusion operation scales like Δy^{-2}. Thus, from Eq. (1), the critical island width W is expected to satisfy $W\sim D^{1/3}$. Numerically, the critical island width may be defined, as suggested by Sovinec *et al.* [36], by the existence of an inflection in the density at the elliptic periodic orbit at the center of the island. Considering the (0, 1) island, with center at $(x,y)=(0,0)$ and width well approximated by $\sqrt{2}W=\sqrt{k}$, the inflection is given when $\rho_s|_{0,1/2}=0$. For a given D, the critical island width is easily determined numerically (see, for example, Fig. 4) and satisfies the expected scaling (Fig. 5).

Given that as D becomes small the density is flattened both along the unstable manifolds and across the islands and that together the islands and the stochastic sea comprise almost all of the computation domain for $k=0.9716$, one may be tempted to conclude that the density flattens across the domain as D becomes small. This cannot be the case here, as the boundary conditions enforce a gradient across the chaotic

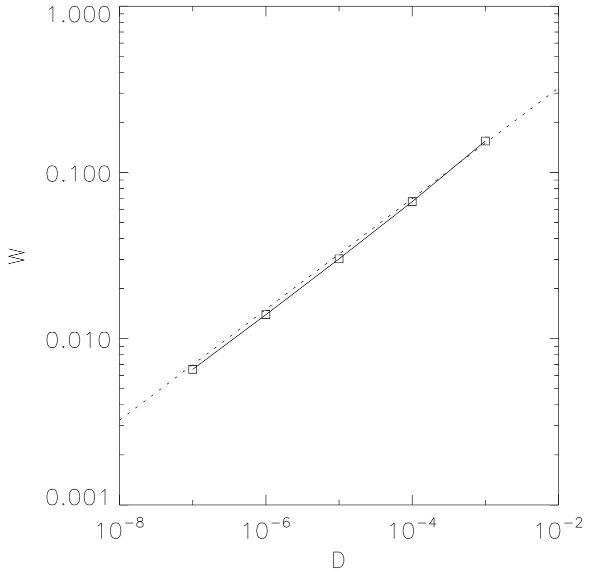

FIG. 5. Critical island width W against diffusion coefficient D. The dashed line satisfies $W=\frac{3}{2}D^{1/3}$

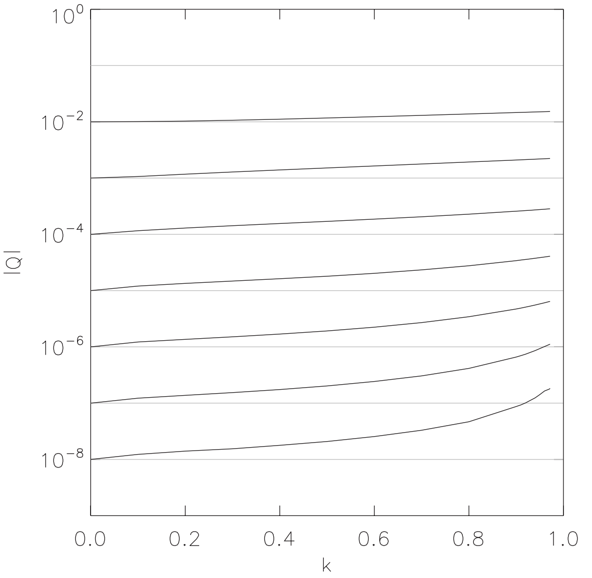

FIG. 6. Particle flux Q as a function of perturbation parameter k, for various values of diffusion D, where $D=|Q(0)|$.

layer. The relevant measure of radial transport is then the particle flux

$$Q=D\int \boldsymbol{\nabla}\rho\cdot\mathbf{n}\sqrt{g}\,d\alpha, \tag{13}$$

where the integral is over the coordinate boundary and $\mathbf{n}$ is normal to the boundary. If there were no barriers to transport within the chaotic layer, the particle flux would become unbounded.

In the integrable case $k=0$, the solution satisfies $\boldsymbol{\nabla}\rho\cdot\mathbf{n}=-1$ on the coordinate boundary and the diffusive flux is $Q=-D$. The particle flux as a function of perturbation parameter k, for various values of D, is shown in Fig. 6. For large D, the steady-state solution is largely independent of the structure of the flow and the chaotic enhancement to the transport is small. For smaller D, where the steady-state solution is closely aligned with the structure of the flow $\mathbf{v}\cdot\boldsymbol{\nabla}\rho\approx 0$, the chaotic enhancement is larger; however, the transport is not without bound. A numerical fit to the particle flux shows that $|Q|\approx\beta D^{1-\gamma}$, where β and γ vary weakly with k: for $k=0$, $\beta=1$, and $\gamma=0$ and for $k=0.9716$, $\beta\approx 0.69$, and $\gamma\approx 0.14$. The increase in the particle flux with k, for a given D, is surprisingly small. The resolution of this apparent paradox is that as D becomes smaller, the system becomes dominantly Hamiltonian, and for Hamiltonian systems the near-critical cantori become extremely effective partial barriers against radial advective transport. (For $D=0$, the steady-state balance between the advection and diffusion is somewhat pathological, as there is no diffusion: there exists no mechanism for particles to deviate from the coordinate boundary.)

To illustrate the relationship between the density contours and the cantori, a set of cantori is constructed (Table I). It is convenient to label the cantori with the continued fraction representation: every irrational number ω may be expressed as [39]

$$\omega=a_0+\cfrac{1}{a_1+\frac{1}{a_2+\cdots}}=[a_0,a_1,a_2,\ldots], \tag{14}$$

where the integers a_j are called the partial quotients. The continued fraction representation of an irrational gives rise to an infinite sequence of partial quotients. By truncating at the jth partial quotient, a rational approximation $p_j/q_j=[a_0,a_1,\ldots,a_j]$, called the jth convergent, to the irrational is obtained. The convergent, action-minimizing periodic orbits form a sequence of consecutively better approximates to the irrational cantorus. Cantori of particular importance are those with noble frequency, where the continued fraction representation terminates with a infinite sequence of 1's, as these

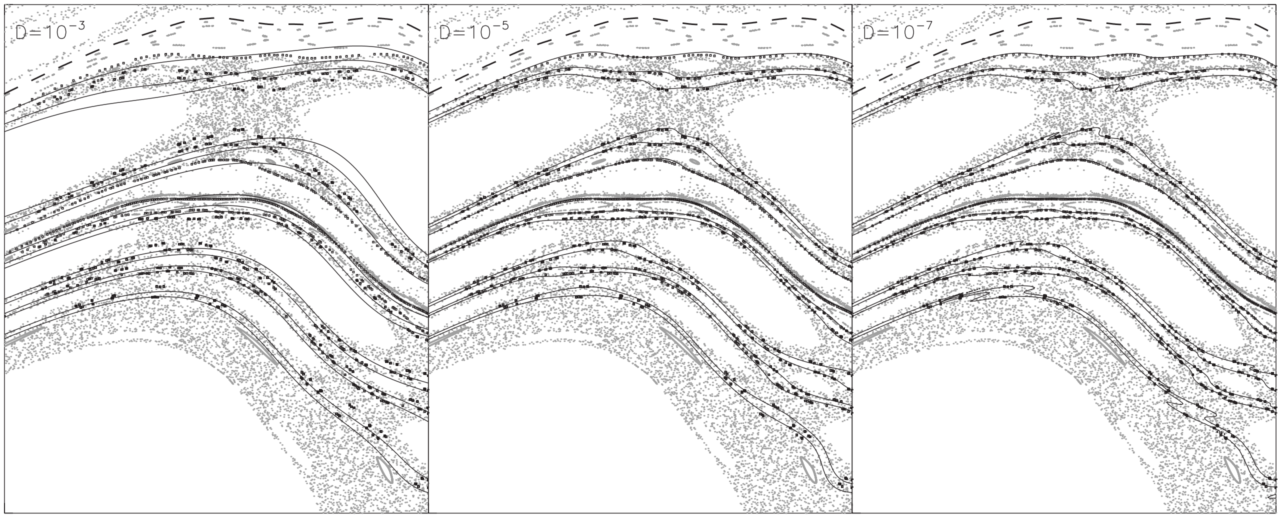

FIG. 7. Poincaré plot showing the stochastic sea (gray dots), the coordinate boundary (dashed curve), the selected cantori (black dots), and the cantori density contours (black lines) for $D=10^{-3}$ (left), $D=10^{-5}$ (middle), and $D=10^{-7}$ (right). The horizontal x axis range is [0.0, 0.5], the vertical y range is [0.1, 0.7], and the perturbation parameter $k=0.9716$.

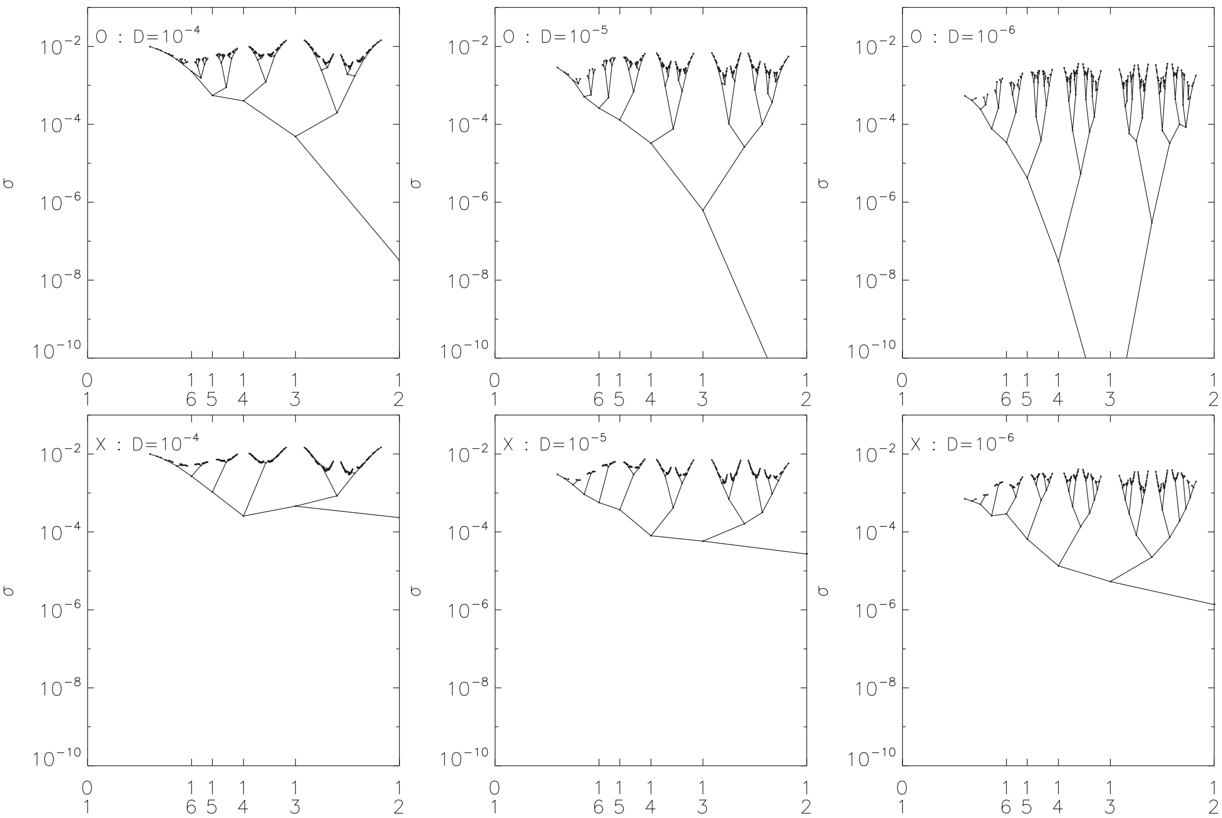

FIG. 8. Variation σ in density ρ along (p,q) periodic orbits, for the first seven levels of the Farey tree, for the perturbation parameter $k=0.9716$, plotted against frequency $\omega=p/q$ for $D=10^{-4}$ (left), $D=10^{-5}$ (middle), and $D=10^{-6}$ (right). The upper (lower) row is for the elliptic (hyperbolic) periodic orbits.

present barriers of locally minimal flux to the radial advective motion [7].

The periodic orbits required for this article are located using action-extremizing techniques, where a Newton method is used to set the action gradient to zero. Each of the selected cantori are approximated by the tenth convergent minimizing, periodic-orbit, $\{(x_i,y_i),\ i=0,\ q-1\}$, as indicated in Table I and plotted in Fig. 7. (Table I also includes the continued fraction representation of the boundary KAM curve.) Contours of the density, the "cantori contours," given by the average density $\langle\rho\rangle=\Sigma_i\rho(x_i,y_i)/q$, are also shown. As the diffusion decreases, the correlation between the density contours and the cantori improves.

TABLE I. Selected cantori and boundary KAM curves.

Continued fraction	ω	(p_5,q_5)	(p_{10},q_{10})
$[0,1,1,1,1^\infty]$	0.61803…		
$[0,1,1,2,1^\infty]$	0.58015…	(7,12)	(76,131)
$[0,1,1,3,1^\infty]$	0.56069…	(9,16)	(97,173)
$[0,1,1,4,1^\infty]$	0.54883…	(11,20)	(18,215)
$[0,2,4,1,1^\infty]$	0.45114…	(14,31)	(57,348)
$[0,2,3,1,1^\infty]$	0.43928…	(11,25)	(23,280)
$[0,2,2,1,1^\infty]$	0.41981...	(8,19)	(89,212)
$[0,2,1,1,1^\infty]$	0.38194…	(5,13)	(55,144)
$[0,2,1,2,1^\infty]$	0.36715…	(7,19)	(76,207)
$[0,2,1,3,1^\infty]$	0.35925…	(9,25)	(97,270)
$[0,3,3,1,1^\infty]$	0.30521...	(11,36)	(23,403)
$[0,3,2,1,1^\infty]$	0.29568...	(8,27)	(89,301)
$[0,3,1,1,1^\infty]$	0.27638...	(5,18)	(55,199)
$[0,3,1,2,1^\infty]$	0.26855...	(7,26)	(76,283)
$[0,4,2,1,1^\infty]$	0.22820...	(8,35)	(89,390)
$[0,4,1,1,1^\infty]$	0.21653...	(5,23)	(55,254)

Cantori are approximated by minimizing periodic orbits, so the density variation on the cantori is approximated by the variation σ on the periodic orbits, where $\sigma=\langle|\rho(x_i,y_i)-\langle\rho\rangle|\rangle$. This quantity is shown (Fig. 8), on a Farey tree [7] of periodic orbits, beginning with the (0, 1) and (1, 2) rationals (level 0). The subsequent levels of the tree are constructed by successively adding the mediants, formed by adding the numerators and denominators of adjacent rationals: e.g., at level 1, (1, 3) is added; at level 2, (1, 4) and (2, 5) are added; etc. With a strong advective coupling along streamlines and weak diffusive coupling across streamlines, it is expected that the "shorter" streamlines will have smaller variation. This is often the case, particularly so for the elliptic periodic orbits. This figure shows that the variation decreases as the diffusion decreases. Also, as the periodic orbits get longer, the variation converges (the branches of the tree get smaller in length), so the cantorus variation limit is well defined. For example, for the convergents to the $[0,3,1^\infty]$ cantorus, the variations $\sigma_{p/q}$ on the minimizing periodic orbits (increased by a factor of 100) for $D=10^{-6}$ are $\sigma_{1/3}=0.001$, $\sigma_{1/4}=0.001$,

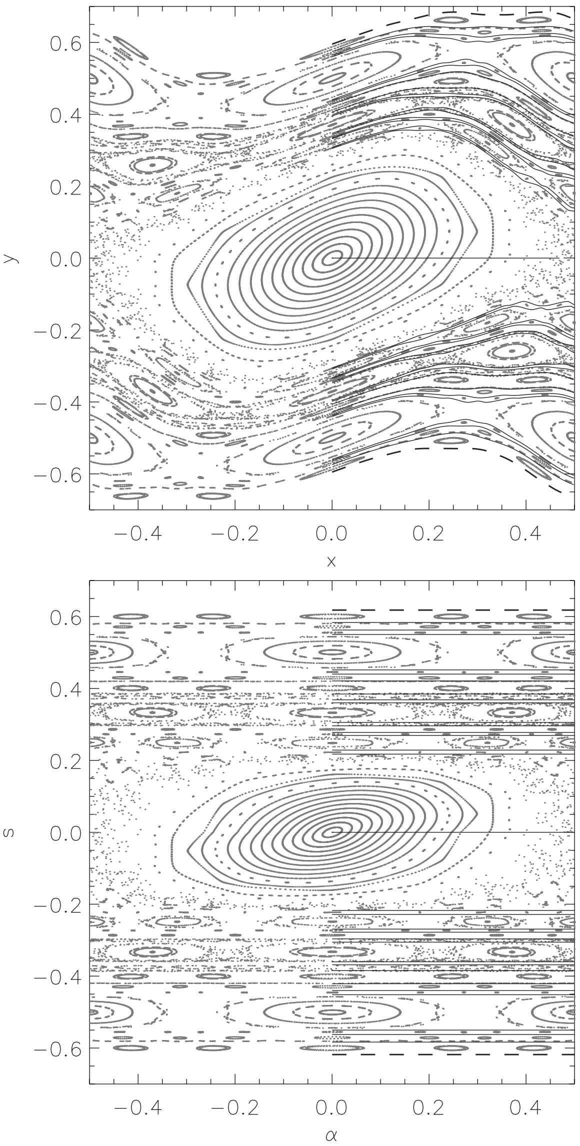

FIG. 9. Poincaré plot (gray dots), selected ghost circles (black curves), and coordinate boundary (dashed curves) in both (x,y) coordinates (above) and (α,s) ghost coordinates (below).

$\sigma_{2/7}=0.013$, $\sigma_{3/11}=0.041$, $\sigma_{5/18}=0.197$, $\sigma_{8/29}=0.220$, $\sigma_{13/47}=0.225$, $\sigma_{21/76}=0.229$, $\sigma_{34/123}=0.229$, and $\sigma_{55/199}=0.229$. This figure also shows that it is not always the case that following an alternating path along this tree reduces the variation, particularly so for the hyperbolic orbits. Alternating paths along the Farey tree converge to noble irrationals, which are associated with the most robust KAM curves and the cantori of minimal advective flux.

In the chaotic regions, points near the hyperbolic orbits may be advectively coupled to regions of phase space with quite different values of density, thus leading to large density gradients and enhanced diffusion. The elliptic orbits are shielded somewhat from the chaos when the size of the island exceeds the critical island width $W \sim D^{1/3}$. One may expect that the stable elliptic orbits have smaller variation than the hyperbolic orbits, and this is confirmed by Fig. 8. Perhaps this argument could be refined to illustrate that the KAM curves, which are approximated by both the elliptic and hyperbolic periodic orbits and where the nearby unstable manifolds have vanishing extent, have locally minimizing variation (and thus justify the imposed boundary condition that the density be constant on the KAM curves taken as the computational boundary). However, when the KAM curves break into cantori, the nearby elliptic orbits become unstable [25] and are no longer insulated from the chaos. Furthermore, it is not the elliptic orbits that approximate cantori, but the hyperbolic orbits.

IV. GHOST CIRCLES AND GHOST COORDINATES

Despite the lack of conclusive evidence, the correlation between the density contours and the cantori shown in Fig. 7 is suggestive that the cantori are important barriers to advective-diffusive transport. This section explores to what extent coordinates adapted to the cantori can be used to organize the dynamics. Coordinate curves may be constructed that fill in the gaps in the cantori [21,40], but there are reasons to believe, as argued by MacKay and Muldoon [27], that curves adapted to the periodic orbits are preferable. Just as in the integrable case, where the (action) coordinate curves are adapted to the curves invariant under the advective flow, here the coordinate curves are adapted to the periodic orbits that approximate the cantori. To do this, it is required to construct a set of "rational" coordinate curves.

It seems a natural criterion that the coordinate curves be required to pass through the periodic orbits, but there is some freedom in how the spaces between the periodic orbits are to be filled. Various rational coordinate curves have been suggested [41]: in particular, *ghost circles* [26,27] and *quadratic-flux minimizing curves* [42]. The continuous-time analog of quadratic-flux-minimizing curves [43,44] has been exploited to simplify the description of perturbed toroidal magnetic fields [45,46]. Here, a coordinate system based on ghost circles is described.

A (p,q) ghost circle is constructed [27] by first locating the minimax periodic orbit, $\{x_i,\ i=0,\ q-1\}$. This is a simple task for the standard map, as the minimax orbits, for $k \geq 0$, lie on the symmetry line $x=0$ [47]. The derivative of the action gradient is a cyclic, tridiagonal matrix $D^2W_{p/q}$ called the Hessian. For the minimax orbits, this matrix generically has a single negative eigenvalue and the corresponding eigenvector $\mathbf{u}$ determines the direction, in configuration space, in which the action decreases. By deforming the set of points $\{x_i,\ i=0,\ q-1\}$ in the direction $\pm\mathbf{u}$, then flowing down the action gradient according to

$$\frac{dx_i}{d\tau} = -\frac{\partial W_{p/q}}{\partial x_i}, \tag{15}$$

the set $\{x_i,\ i=0,\ q-1\}$ will evolve, with decreasing action, into the minimizing orbit and in doing so will trace out a smooth curve, a ghost circle. Different ghost circles, as identified by their periodicity, are disjoint and are graphs over x [27] (each vertical line $x=\text{const}$ passes through each curve only once). A continuous coordinate system, "ghost coordinates," is constructed by radially interpolating between a fi-

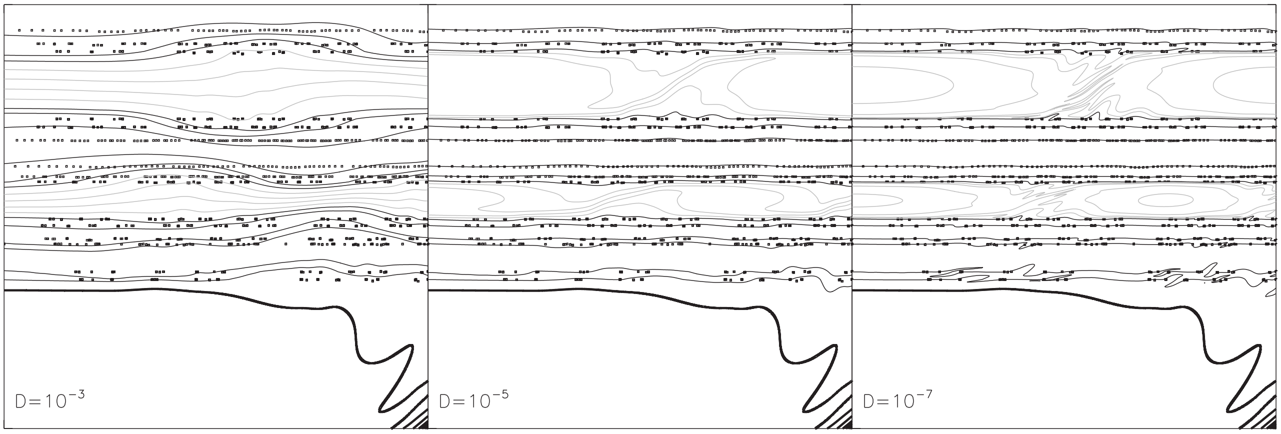

FIG. 10. Density contours (gray lines), selected cantori (black dots), and the average cantori density contours (black lines) plotted in ghost coordinates for $D=10^{-3}$ (left), $D=10^{-5}$ (middle), and $D=10^{-7}$ (right). The horizontal α range is [0.0, 0.5], the vertical y range is [0.0, 0.61803], and the perturbation parameter $k=0.9716$. The thick black line is the (0,1) unstable manifold.

nite set of ghost circles. The "upward" advective flux across the rational ghost circle (in fact, for any curve connecting the minimax and minimizing orbits) is given by the difference in action between these periodic orbits [7].

The selection of which ghost circles to use as the coordinate framework is arbitrary and depends on the application. Here a set is chosen with periodicity given by the fifth convergent of the selected cantori, given in Table I. These ghost circles are shown in Fig. 9. Although these seem rather low-order approximates to the irrational cantori, which formally have $q=\infty$, the fact that the cantori exhibit a strong clustering [22,25] near the low-order periodic orbits allows them to be approximated by low-order ghost circles.

The integration parameter τ in Eq. (15) is arbitrary. The angle α parametrization, given by

$$\frac{d\alpha}{d\tau}=\sum_{i=0}^{q-1}\frac{1}{q}\frac{dx_i}{d\tau}, \tag{16}$$

reduces to the rigid rotation angle in the integrable case. This angle reduces the motion in periodic orbits to simple linear motion. However, because of the strong clustering, the high-order periodic orbits are not evenly spaced in x and forcing the gaps between the periodic orbits to be equal in α causes the ghost coordinates to become highly irregular. While this is no problem for the ghost circles themselves, and ghost circles of arbitrarily high order may be constructed, difficulties are encountered in the subsequent interpolation. Here the angle $\alpha=x$ is used and, because the ghost circles are graphs over x, an extension of the simple linear interpolation, Eq. (5), ensures that the interpolated coordinate curves do not intersect.

A Poincaré plot of the advective flow (the standard map) is shown (Fig. 9), in both (x,y) and ghost coordinates. That the selected cantori lie close to coordinate curves is displayed in Fig. 10, which also shows the steady-state density contours in ghost coordinates. By plotting the cantori density contours, one can see that the constructed ghost coordinates regularize the dynamics in regions where the cantori dominate the transport. In this figure, the (0, 1) unstable manifold is also shown. Additional density contours are plotted across the (1, 3) and (1, 2) islands, where the influence of the (1, 3) and (1, 2) unstable manifolds can be seen.

By employing a coordinate system adapted to the chaotic structure of the flow, the solution for small but nonzero diffusion has been partitioned into regions of rapid mixing and density flattening associated with (rational) islands and unstable manifolds and regions of dominantly regular motion and density gradients where transport is restricted by (irrational) cantori. This gives the density profile (averaged over α) the structure of a smoothed devil's staircase [28] (Fig. 11).

The devil's staircase, also called Cantor's function C, is constructed here in a similar fashion to the common example of a Cantor set. Starting with the interval [0, 1], the open middle third $\left(\frac{1}{3},\frac{2}{3}\right)$ is deleted. In this deleted interval, the Cantor function $C(\omega)$ is set to the midpoint of the deleted interval—that is, for $\omega\in\left(\frac{1}{3},\frac{2}{3}\right)$ we have $C(\omega)=\frac{1}{2}$. This is repeated in the remaining intervals $\left[0,\frac{1}{3}\right]$ and $\left[\frac{2}{3},1\right]$. The next deleted sets are $\left(\frac{1}{9},\frac{2}{9}\right)$ and $\left(\frac{7}{9},\frac{8}{9}\right)$, and the Cantor function in these intervals is $C=\frac{1}{4}$ and $C=\frac{3}{4}$, respectively. By continuing this process indefinitely, one arrives at the Cantor function. The remaining set, comprised of all the points that are never deleted (such as the end points $\frac{1}{3}$, $\frac{2}{3}$, $\frac{1}{9}$, $\frac{2}{9}$, etc.), is a Cantor set.

It is interesting that Cantor sets, the cantori, give rise to a density profile with the structure of a smoothed Cantor function. It is not the case that the density profile will agree exactly with the devil's staircase as shown. The figure is intended to illustrate that the fractal properties of the density profile are similar to the fractal structure of the staircase, with the diffusion providing smoothing. A detailed study of the smoothed staircase structure of the density profile will be given elsewhere.

V. COMMENTS

Ghost coordinates represent a natural extension of the concept of action-angle coordinates to Hamiltonian chaotic

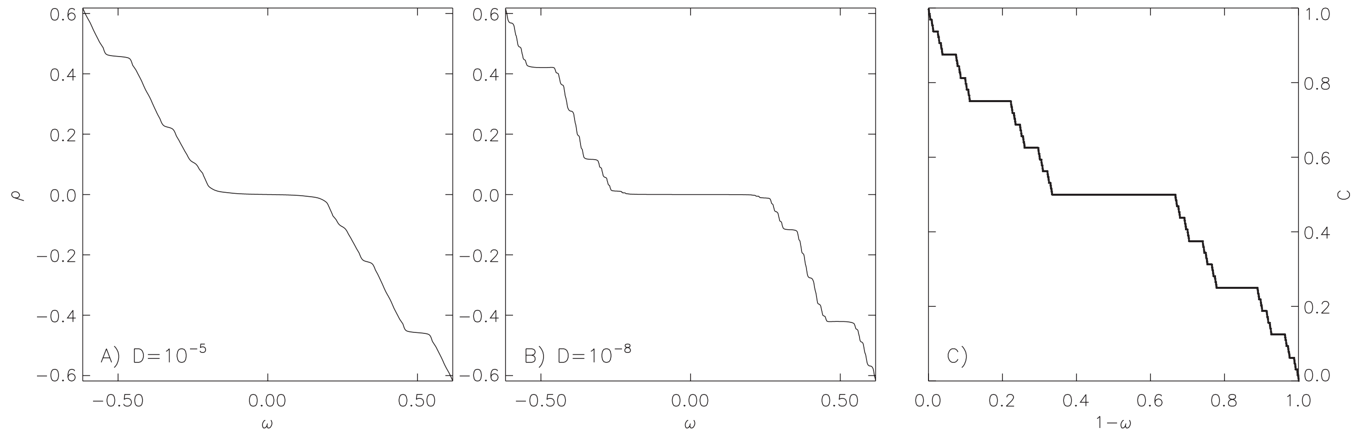

FIG. 11. Radial density profiles, for $D=10^{-5}$ (left) and $D=10^{-8}$ (middle), in ghost coordinates for the perturbation parameter $k=0.9716$, compared to the devil's staircase function C (right).

flows. They are adapted to invariant remnants of the advective flow, the periodic orbits, and by constructing ghost circles of increasingly high periodicity, the irrational invariant sets—i.e., the cantori—coincide with coordinate curves. The above results suggest that cantori are the most significant barriers to advective-diffusive transport in chaotic systems and that the "chaotic" ghost coordinates naturally reveal the smoothed devil's staircase structure of the solution.

To resolve more details of the devil's staircase structure, the ghost coordinates can be adapted to additional cantori. Formally, the devil's staircase is discontinuous. This corresponds to the limit $D=0$, in which case the KAM surfaces, if any are present, present complete barriers to transport and can thus support discontinuous density profiles. The cantori, however, are leaky, partial barriers. Streamlines can pass across the cantori, and thus presumably in this limit the cantori cannot sustain sharp density drops. In this case, however, the density is a fractal: the density is constant along each of the infinitely many unstable manifolds that comprise the stochastic sea, and the densities on different streamlines have no interaction. In this case, sharp density drops can be sustained almost everywhere in the chaotic sea.

With small diffusion, the extent to which cantori can support density gradients is presumably determined by the level of advective flux across the cantori: the smaller the advective flux, the greater the density gradient that can be supported. Near-critical cantori and KAM curves will be similarly effective barriers against transport.

This work is somewhat incomplete. A more careful investigation of the structure of the periodic orbits, with an analysis incorporating the advective-diffusive length scale, may allow some universal statements regarding steady-state solutions to advective-diffusive transport in a wider class of chaotic flows. In this article we have not comprehensively demonstrated that cantori are the most effective barriers against advective-diffusive transport, but they are the most important barriers against purely advective transport, when $D=0$, and they clearly play a similarly important role when D is small. Hopefully, this work will serve as a basis for future investigations.

Finally, a natural extension of this work is to continuous-time flows, perhaps to study the effect of cantori on heat and particle transport in the partially stochastic magnetic fields relevant to plasma confinement devices [48]. The Hamiltonian flow in this case could be provided by the guiding center drift Hamiltonian [49,50]. More substantial numerical and experimental investigations may show that cantori play an important role in restricting transport in magnetically confined plasmas.

ACKNOWLEDGMENTS

I would like to thank Neil Pomphrey, Ravi Samtaney, Roscoe White, Allen Boozer, and Don Monticello for rewarding discussions. This work was supported in part by U.S. Department of Energy Contract No. DE-AC02-76CH03073 and Grant No. DE-FG02-99ER54546.

[1] C. Eckart, J. Mar. Res. **7**, 265 (1948).
[2] J. Moser, *Stable and Random Motions* (Princeton University Press, Princeton, NJ, 1973).
[3] V. I. Arnold, *Mathematical Methods of Classical Mechanics* (Springer-Verlag, New York, 1978).
[4] A. J. Lichtenberg and M. A. Lieberman, *Regular and Chaotic Dynamics*, 2nd ed. (Springer-Verlag, New York, 1992).
[5] D. K. Arrowsmith and C. M. Place, *An Introduction to Dynamical Systems* (Cambridge University Press, Cambridge, England, 1991).
[6] H. Goldstein, *Classical Mechanics*, 2nd ed. (Addison-Wesley, Reading, MA, 1980).
[7] J. D. Meiss, Rev. Mod. Phys. **64**, 795 (1992).
[8] S. R. Hudson, Phys. Plasmas **11**, 677 (2004).
[9] H. Poincaré, in *Les Méthodes nouvelles de la Mécanique celeste* (Gauthier-Villars, Paris, 1892), Pts. 1, 2, and 3; *History of*

Modern Physics and Astronomy, edited by D. L. Goroff (AIP, New York, 1993), Vol. 13.

[10] V. Rom-Kedar and S. Wiggins, Arch. Ration. Mech. Anal. **109**, 239 (1990).

[11] V. Rom-Kedar and S. Wiggins, Physica D **51**, 248 (1991).

[12] H. Aref, J. Fluid Mech. **143**, 1 (1984).

[13] D. Beigie, A. Leonard, and S. Wiggins, Nonlinearity **4**, 775 (1991).

[14] D. Beigie, A. Leonard, and S. Wiggins, Chaos, Solitons Fractals **4**, 749 (1994).

[15] V. Rom-Kedar and A. C. Poje, Phys. Fluids **11**, 2044 (1999).

[16] T. E. Evans, R. A. Moyer, P. R. Thomas, T. E. Evans, R. A. Moyer, P. R. Thomas, J. G. Watkins, T. H. Osborne, J. A. Boedo, E. J. Doyle *et al.*, Phys. Rev. Lett. **92**, 235003 (2004).

[17] I. C. Percival, in *Nonlinear Dynamics and the Beam-Beam Interaction*, edited by M. Month and J. C. Herra, AIP Conf. Proc. No. 57 (AIP, New York, 1979).

[18] S. Aubry and P. Y. Le Daeron, Physica D **8**, 381 (1983).

[19] J. N. Mather, Topology **21**, 457 (1982).

[20] R. S. MacKay, J. D. Meiss, and I. C. Percival, Phys. Rev. Lett. **52**, 697 (1984).

[21] R. S. MacKay, J. D. Meiss, and I. C. Percival, Physica D **13**, 55 (1984).

[22] W. Li and P. Bak, Phys. Rev. Lett. **57**, 655 (1986).

[23] H. J. Schellnhuber and H. Urbschat, Phys. Rev. A **38**, 5888 (1988).

[24] B. Chirikov, Phys. Rep. **52**, 263 (1979).

[25] J. M. Greene, J. Math. Phys. **20**, 1183 (1979).

[26] C. Golé, J. Differ. Equations **97**, 140 (1992).

[27] R. S. MacKay and M. R. Muldoon, Phys. Lett. A **178**, 245 (1993).

[28] P. Bak, Phys. Today **39** (12), 38 (1986).

[29] H. J. Schellnhuber, H. Urbschat, and A. Block, Phys. Rev. A **33**, 2856 (1986).

[30] S. R. Hudson, Phys. Rev. E **74**, 056203 (2006).

[31] J. E. Howard and J. Humphreys, Physica D **80**, 256 (1995).

[32] D. del Castillo-Negrete and P. J. Morrison, Phys. Fluids A **5**, 948 (1993).

[33] W. H. Press, B. P. Flannery, S. A. Teukolsky, and W. T. Vetterling, *Numerical Recipes in Fortran 77: The art of scientific computing*, 2nd ed. (Cambridge University Press, Cambridge, England, 1992).

[34] S. Günter, Q. Yu, J. Krüger, and K. Lackner, J. Comput. Phys. **209**, 354 (2005).

[35] T. Tsai, J. Yang, and L. Huang, Commun. Numer. Methods Eng. **17**, 701 (2001).

[36] C. R. Sovinec, T. A. Gianakon, E. D. Held, S. E. Kruger, and D. D. Schnack, Phys. Plasmas **10**, 1727 (2003).

[37] R. Grima and T. J. Newman, Phys. Rev. E **70**, 036703 (2004).

[38] H. van der Vorst, *Iterative Krylov Methods for Large Linear Systems* (Cambridge University Press, Cambridge, England, 2003).

[39] I. Niven, *Irrational Numbers* (Mathematical Association of America, New York, 1956).

[40] R. S. MacKay, J. D. Meiss, and I. C. Percival, Physica D **27**, 1 (1987).

[41] R. L. Dewar and A. B. Khorev, Physica D **85**, 66 (1995).

[42] R. L. Dewar and J. D. Meiss, Physica D **57**, 476 (1992).

[43] R. L. Dewar, S. R. Hudson, and P. Price, Phys. Lett. A **194**, 49 (1994).

[44] S. R. Hudson and R. L. Dewar, J. Plasma Phys. **56**, 361 (1996).

[45] S. R. Hudson and R. L. Dewar, Phys. Plasmas **6**, 1532 (1999).

[46] S. R. Hudson, D. A. Monticello, A. H. Reiman, A. H. Boozer, D. J. Strickler, S. P. Hirshman, and M. C. Zarnstorff, Phys. Rev. Lett. **89**, 275003 (2002).

[47] H. Kook and J. D. Meiss, Physica D **35**, 65 (1989).

[48] A. Runov, S. Kasilov, R. Schneider, and D. Reiter, Contrib. Plasma Phys. **44**, 18 (2004).

[49] R. G. Littlejohn, Phys. Fluids **24**, 1730 (1981).

[50] R. G. Littlejohn, J. Plasma Phys. **29**, 111 (1983).